JCB Journal of Cell Biology

ARTICLE

Vimentin protects cells against nuclear rupture and DNA damage during migration

Alison E. Patteson[1,2*], Amir Vahabikashi[3*], Katarzyna Pogoda[1,4], Stephen A. Adam[3], Kalpana Mandal[1], Mark Kittisopikul[3], Suganya Sivagurunathan[3], Anne Goldman[3], Robert D. Goldman[3], and Paul A. Janmey[1,5]

Mammalian cells frequently migrate through tight spaces during normal embryogenesis, wound healing, diapedesis, or in pathological situations such as metastasis. Nuclear size and shape are important factors in regulating the mechanical properties of cells during their migration through such tight spaces. At the onset of migratory behavior, cells often initiate the expression of vimentin, an intermediate filament protein that polymerizes into networks extending from a juxtanuclear cage to the cell periphery. However, the role of vimentin intermediate filaments (VIFs) in regulating nuclear shape and mechanics remains unknown. Here, we use wild-type and vimentin-null mouse embryonic fibroblasts to show that VIFs regulate nuclear shape and perinuclear stiffness, cell motility in 3D, and the ability of cells to resist large deformations. These changes increase nuclear rupture and activation of DNA damage repair mechanisms, which are rescued by exogenous reexpression of vimentin. Our findings show that VIFs provide mechanical support to protect the nucleus and genome during migration.

Introduction

The proper function and homeostasis of tissues depend on the ability of individual cells to withstand demanding physical stresses. For example, during migration, a cell must squeeze through small interstitial spaces in tissues, imposing large strains on entire cell bodies and their largest organelle, the nucleus. Determining how cells maintain their structural integrity under these large strains is an important prerequisite for understanding a wide range of normal physiological activities, including tissue morphogenesis during development, wound healing, diapedesis, and pathological conditions such as cancer cell metastasis and chronic inflammatory diseases such as arthritis.

The deformability of cells depends largely on the cytoskeleton, which comprises three main polymers: F-actin, microtubules, and intermediate filaments (IFs). F-actin and microtubules are highly conserved in eukaryotic cells and single-celled organisms, but IFs are diverse and evolved later as multicellular organisms appeared. IFs are classified into five types based on similarities in sequence, which reflect similarities in tissue origin (Lodish et al., 2000; Herrmann and Aebi, 2016). Vimentin is a type III IF protein, and it has been used extensively as a reliable marker of epithelial-to-mesenchymal transition, in which nonmigratory epithelial cells lose cell–cell adhesions, dramatically alter their shape, and transition to a highly migratory mesenchymal phenotype (Yang and Weinberg, 2008; Thiery et al., 2009; Hay, 2005; Mendez et al., 2010). Furthermore, vimentin intermediate filaments (VIFs) are implicated in the development of multiple cancers, and the expression of vimentin is a clinical marker of poor prognosis and increased metastasis (Satelli and Li, 2011). Yet, little is known regarding the role of VIF in 3D cell motility.

The VIF network extends throughout the cytoplasm, from the nucleus surface to the plasma membrane, helping to position the nucleus (Dupin et al., 2011) and other organelles (Guo et al., 2013; Nekrasova et al., 2011). One robust feature of the organization of VIFs is their assembly into an intricate cage-like network that surrounds the nucleus (Lowery et al., 2015). Even under conditions in which the peripheral VIF network is dynamic, such as during growth on soft substrates, the perinuclear VIF cage remains intact (Murray et al., 2014). There is evidence that VIFs establish indirect physical connections to the outer nuclear membrane through interactions with the linker of the nucleoskeleton and cytoskeleton (LINC) complex (Ketema et al., 2013). The LINC complex has also been shown to connect to the nuclear lamina, a thin filamentous layer surrounding the nuclear periphery that is mainly composed of the type V IF proteins, the nuclear lamins (Burke and Stewart, 2014; Dechat et al., 2010).

[1]Institute for Medicine and Engineering, University of Pennsylvania, Philadelphia, PA; [2]Physics Department, Syracuse University, Syracuse, NY; [3]Department of Cell and Molecular Biology, Feinberg School of Medicine, Northwestern University, Chicago IL; [4]Institute of Nuclear Physics, Polish Academy of Sciences, PL-31342 Krakow, Poland; [5]Department of Physiology, University of Pennsylvania, Philadelphia, PA.

*A.E. Patteson and A. Vahabikashi contributed equally to this paper; Correspondence to Paul A. Janmey: janmey@mail.med.upenn.edu; r-goldman@northwestern.edu.

There is considerable evidence that the nuclear lamina plays an important role in determining nuclear shape and rigidity (Lammerding et al., 2006; Stephens et al., 2017; Dahl et al., 2005; Swift et al., 2013; Broers et al., 2004). Changing the expression patterns of specific lamin isoforms alters nuclear shape and the lamin meshwork structure (De Vos et al., 2011; Lammerding et al., 2006; Shimi et al., 2008) and can lead to nuclear abnormalities, such as blebs, in which the lamin B isoforms are depleted (Shimi et al., 2008). Nuclear blebs can also occur spontaneously during cell migration through confined spaces (Denais et al., 2016; Raab et al., 2016). Blebbing can lead to rupture of the nuclear envelope (NE), unregulated mixing of the nuclear and cytosolic materials, accumulated DNA damage, and genomic instability (Irianto et al., 2017).

Previous experiments have shown that IFs play an important role in regulating the transmission of forces to the NE (Maniotis et al., 1997; Neelam et al., 2015). They are major components of the cytoskeletal linkages that directly transfer forces applied at the cell surface to the nucleus (Maniotis et al., 1997). Recent investigations have shown that VIFs also contribute to nuclear homeostasis by providing a stiff elastic response against localized forces (Neelam et al., 2015). These functions are consistent with the mechanical properties of reconstituted VIF networks. VIFs are elastic biopolymers that stiffen at large strains. Unlike cross-linked actin or microtubules, they are capable of withstanding extreme deformations without breakage (Janmey et al., 1991; Kreplak et al., 2005). Based on these findings, our central hypothesis is that the VIF perinuclear cage provides a protective structure that resists extreme deformations to maintain the structural integrity of the nucleus during 3D migration. Here, we investigate the effects of VIF on nuclear morphology and stability in cells grown on conventional 2D rigid substrates and in 3D confining environments, where squeezing of the cells through small pores can lead to large nuclear deformations and damage (Denais et al., 2016; Raab et al., 2016; Irianto et al., 2017).

Results

VIFs surround the cell nucleus, and their depletion perturbs nuclear shape and volume

We used confocal microscopy to examine the structure of the VIF network around the nucleus in vim$^{+/+}$ mouse embryonic fibroblasts (mEFs). The confocal stacks captured at the basal (Fig. 1 a) and apical (Fig. 1 b) nuclear surfaces show the proximity between the VIFs and the nuclear surface. The reconstructed 3D renderings of the confocal stacks further show that VIFs are closely juxtaposed to the nuclear surface, frequently appearing as a cage-like filamentous network surrounding it (Fig. 1 c). Details of the VIF cage in close association with the NE are also shown by structured illumination microscopy (SIM) in a vim$^{+/+}$ mEF at the basal surface (Fig. 1 d), at the apical surface (Fig. 1 e), and in a maximum projection (Fig. 1 f).

Fig. 2 demonstrates that the VIF network in vim$^{+/+}$ mEFs (Fig. 2 a) is missing in vim$^{-/-}$ mEFs (Fig. 2 b). The reintroduction of exogenous wild-type vimentin in vim$^{-/-}$ mEFs (which we refer to as "rescued") results in the expression of vimentin to the levels seen in vim$^{+/+}$ cells, as determined by immunoblotting (Fig. S1). The rescued mEFs assemble into a normal VIF network (Fig. 2 c) extending from the perinuclear region to the cell surface (Fig. 2, d–f).

To quantify the properties of the vimentin cage, we measured the intensity of immunofluorescence labeling of vimentin as a function of lateral distance from the nucleus as well as the angle around the centroid of the nucleus (Fig. 3). We identified a consistent intensity pattern within 1 µm of the nucleus in the vim$^{+/+}$ mEFs and observed similar phenomena in the rescued cells (Fig. 3, a and b). To test if the vimentin cage in the rescued cells resembled the cage in the vim$^{+/+}$ cells, we performed circular statistics on the intensity pattern within 1 µm of the nucleus. In particular, we calculated the circular variance (Berens, 2009) to measure the dispersion of the fluorescence intensity distribution around the nucleus (Fig. 3, c–f). The circular variance is normalized such that the nondimensional value ranges from 0 (directed) to 1 (uniform). We found that the vimentin cages within 1 µm had a median circular variance of 0.84 in the wild type and 0.91 in the rescue, suggesting that the vimentin cages tended to be more uniformly distributed around the nucleus in the rescued cells (Fig. 3 g). Furthermore, we performed a Wilcoxon rank sum test and determined that the distributions of circular variance were significantly different between the vim$^{+/+}$ and rescued cells. These results show that the rescued cells were able to successfully express vimentin and form perinuclear structures that exceed the uniformity of the vim$^{+/+}$ cages within 1 µm of the nucleus. In other words, despite ectopic expression from a distinct promoter, pCMV (cytomegalovirus promoter), vimentin in the rescue cells was able, first, to reconstitute the perinuclear cage, and second, to surround the nucleus more completely than in wild type. Overall, we found that both vim$^{+/+}$ and rescued cells consistently formed vimentin cages of ≥1 µm in thickness that surround the nucleus.

Given the proximity of the VIF cage to the nuclear surface and the known strain-stiffening properties of VIF, we determined whether it is involved in regulating nuclear shape. To this end, we compared nuclear profiles in vim$^{+/+}$ and vim$^{-/-}$ mEFs. The nuclei in vim$^{+/+}$ mEFs adhering to a flat rigid surface typically possess an oblate spheroidal shape. In contrast, the nuclei in vim$^{-/-}$ mEFs show an altered shape, looking significantly rounder compared with the vim$^{+/+}$ mEFs (Fig. 4 a). To quantify these changes in nuclear shape, we calculated the sphericity of the nuclei in vim$^{+/+}$, vim$^{-/-}$, and rescued mEFs. The sphericity analysis showed that the nuclei in vim$^{+/+}$ mEFs are flatter and more elliptical in shape compared with the vim$^{-/-}$ mEFs, which have rounder nuclei (Fig. 4 b, $P < 0.007$). Expressing exogenous wild-type vimentin in the vim$^{-/-}$ mEFs restored the average nuclear shape phenotype in rescued mEFs (Fig. 4 b, $P < 3 \times 10^{-7}$).

The shape of the nucleus is correlated with the shape of the cell. On 2D substrates, the nucleus becomes more compressed as the cell spreading area increases (Li et al., 2015; Lele et al., 2018; Sarria et al., 1994). This has led to a model suggesting that nuclear shape is regulated by compressive forces generated by the actomyosin-rich cell cortex and transmitted to the nucleus (Li et al., 2015; Lele et al., 2018; Sarria et al., 1994). A further extension of this model suggests that nuclear compression is mediated by changes in cell spreading and the transmission of force

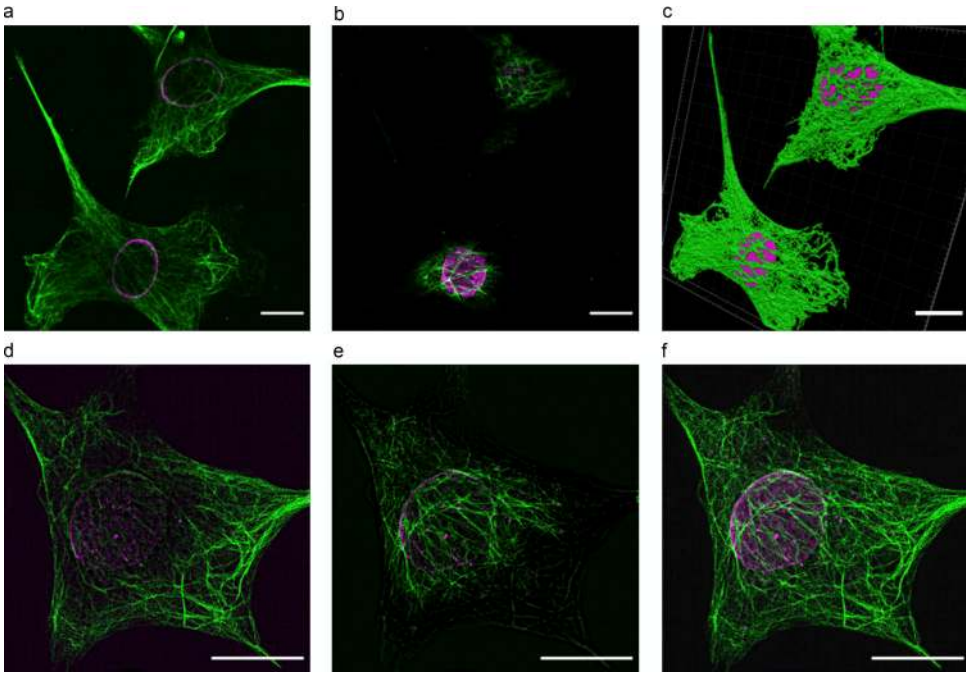

Figure 1. **Perinuclear cage of VIF. (a–c)** Confocal images of the VIFs (green) at the lower (a) and upper (b) surfaces of the nuclei (magenta) and their 3D rendering (c) in two vim$^{+/+}$ mEFs. **(d and e)** SIM images of the vimentin cage around the nucleus (magenta) in a vim$^{+/+}$ mEF at the basal (d) and apical (e) surfaces of the nucleus. **(f)** Maximum projection of SIM images for the cell in d and e. Scale bar is 20 µm.

from the moving cell boundaries to the nuclear surface, also by actomyosin located in the cell cortex (Li et al., 2015; Lele et al., 2018). Based on these findings, we determined if the altered nuclear shape in vim$^{-/-}$ mEFs could be related to cell spreading. We measured the area of spread vim$^{+/+}$ and vim$^{-/-}$ mEFs by tracing the cortical actin at the cell periphery as marked by phalloidin staining (Fig. S2, a and d). Fig. 4 c shows that vim$^{-/-}$ cells have a significantly smaller spread area compared with vim$^{+/+}$ cells ($P < 0.0005$). We next used multiple linear regression analyses to examine the effect of vimentin (presence or

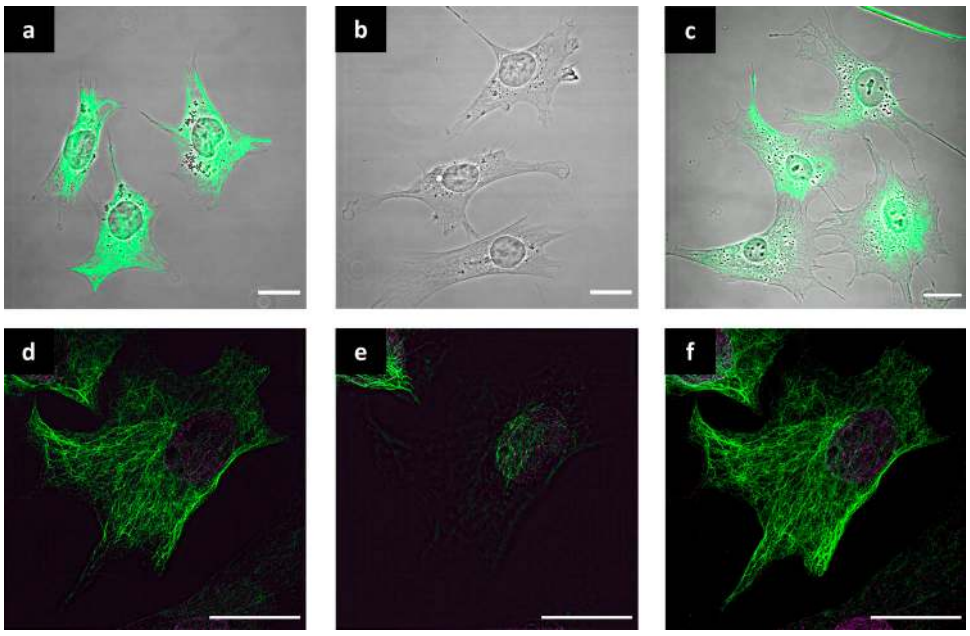

Figure 2. **Overall distribution of VIF in vim$^{+/+}$, vim$^{-/-}$, and rescued mEFs. (a–c)** Immunofluorescence (maximum-intensity projection of confocal stacks)/phase-contrast images of vimentin (green) in vim$^{+/+}$ (a), vim$^{-/-}$ (b), and rescued mEFs expressing exogenous wild-type vimentin (c). **(d and e)** SIM images of the vimentin cage around the nucleus (magenta) in a rescued mEF at its basal (d) and apical (e) planes. **(f)** Maximum projection of the SIM images for the cell in d and e. Scale bar is 20 µm.

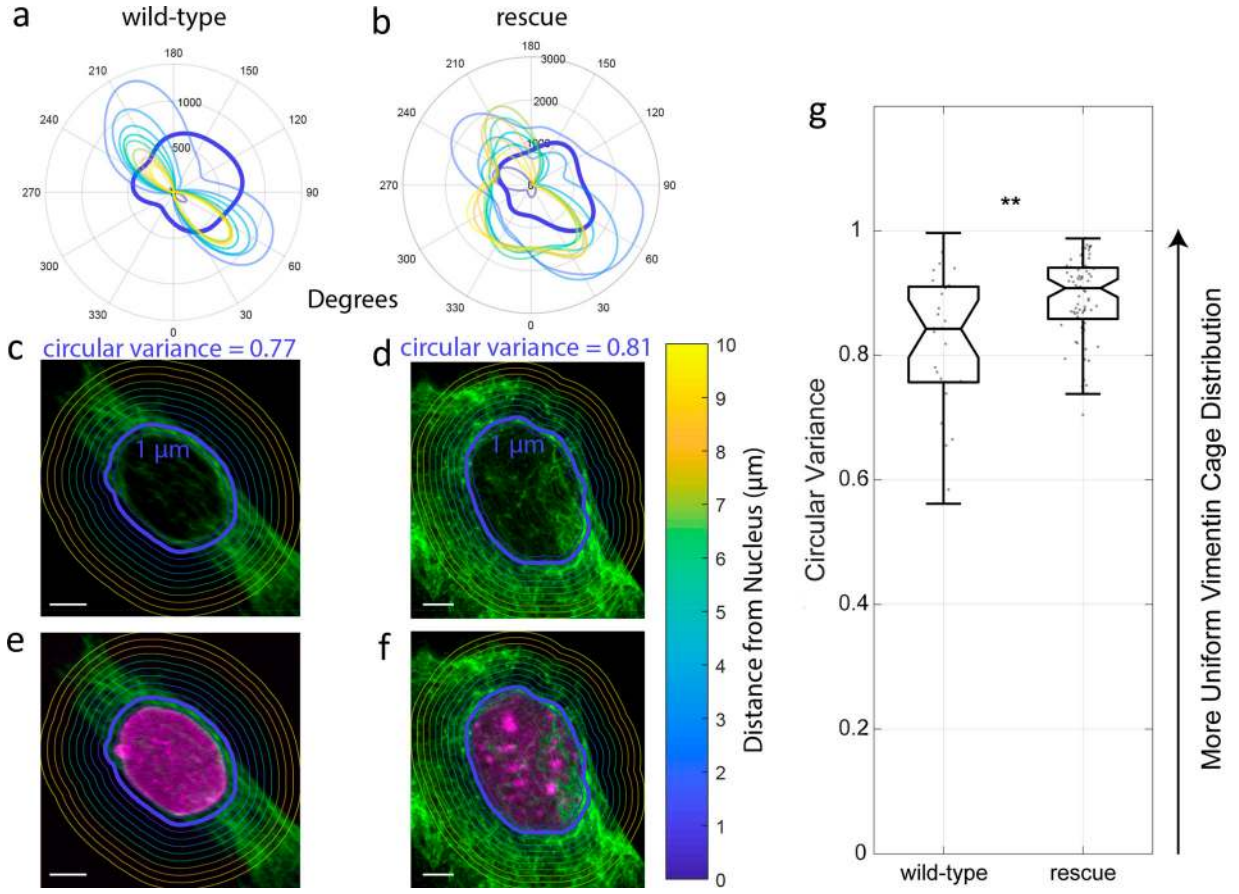

Figure 3. **Quantification of VIF distribution in the perinuclear region. (a and b)** Examples of polar histogram plots of a moving average of fluorescence intensity at 1-µm intervals around the nucleus of a vim$^{+/+}$ (a) and a rescued (b) mEF. Distance from the origin indicates averaged fluorescence intensity, while the angle of the intensity is indicated in degrees. The thick blue line indicates the fluorescence intensity at a distance of 1 µm from the nucleus. Other lines indicate fluorescence intensity at the distances corresponding to the color bar. **(c–f)** Examples of the outer boundaries of the ring-like regions around the nucleus. **(c and d)** The observed vimentin immunofluorescence in green from confocal imaging of the vim$^{+/+}$ and rescued cells, respectively. The blue text indicates the circular variance of the vimentin immunofluorescence intensity bounded by the thick blue line. **(e and f)** Merges in the lamin stain of the nucleus in magenta. **(g)** The distribution of circular variance in the vim$^{+/+}$ and rescue cells using box plots (the number of samples from a single pair of experiments is shown at the bottom: wild-type, n = 27; rescue, n = 77). The thick horizontal line indicates the location of the median. The lower and upper parts of the box represent the 25th and 75th percentiles. The ends of the notch indicate 1.57 times the interquartile range divided by the square root of the number of samples. The whiskers indicate the range of the circular variance up to 1.5 times the interquartile range away from the quartiles. Scale bar is 20 µm.

absence) and cell spreading area on nuclear sphericity. The results indicate that there is a significant effect of cell spreading on nuclear sphericity ($P < 3 \times 10^{-7}$). The greater cell spreading area is correlated with flatter and more elliptically shaped nuclei. Also, the effect of cell spreading is significantly different between the vim$^{+/+}$ and vim$^{-/-}$ mEFs ($P < 0.0003$). We further compared the elongated shape of the vim$^{+/+}$ and vim$^{-/-}$ mEFs to test whether there are notable changes in cell shape in vim$^{-/-}$ mEFs compared with vim$^{+/+}$ cells. To this end, we compared the aspect ratio in the two cell types (Fig. 4 d) and found no significant difference. Therefore, the altered nuclear shape in vim$^{-/-}$ cells cannot be explained simply by differences in the overall cell shape.

We next used confocal stacks to generate 3D renderings of the nuclei to calculate their corresponding volumes in vim$^{+/+}$, vim$^{-/-}$, and rescued mEFs. The average nuclear volume in the vim$^{-/-}$ MEFs was ∼20% smaller than those of the vim$^{+/+}$ and rescued mEFs ($P < 4 \times 10^{-7}$, Fig. 4 e). There was no difference in volume between the vim$^{+/+}$ and rescued mEFs ($P = 0.45$). Similar results were obtained for the cell volume, where the averages obtained for vim$^{+/+}$ and rescued mEFs were significantly greater than that of the vim$^{-/-}$ mEFs ($P < 0.0004$, Fig. 4 f), and the average cell volumes were not different between the vim$^{+/+}$ and rescued mEFs ($P = 0.5$). We also found a significant linear correlation between the nucleus and cell volume in all cell types examined ($P < 10^{-8}$, Fig. 4 g). The regression slope for the vim$^{-/-}$ mEFs (slope = 7.5) was significantly different ($P < 0.035$) from that $r(\theta)$ of the vim$^{+/+}$ mEFs (slope = 9.1).

We then sought to quantify the structure of the nucleus by tracing the nuclear contour and calculating the mean-square amplitude of the Fourier modes of nuclear shape u_q^2 as described in Materials and methods (Fig. 4 h). We found that the contour of the nucleus was smoother in vim$^{+/+}$ mEFs compared with vim$^{-/-}$ cells. The mean squared amplitude decays with wave number q, scaling as $u_q^2 \sim q^{-2}$, which is similar to tension-suppressed fluctuation in lipid membranes (Sackmann, 1994), a

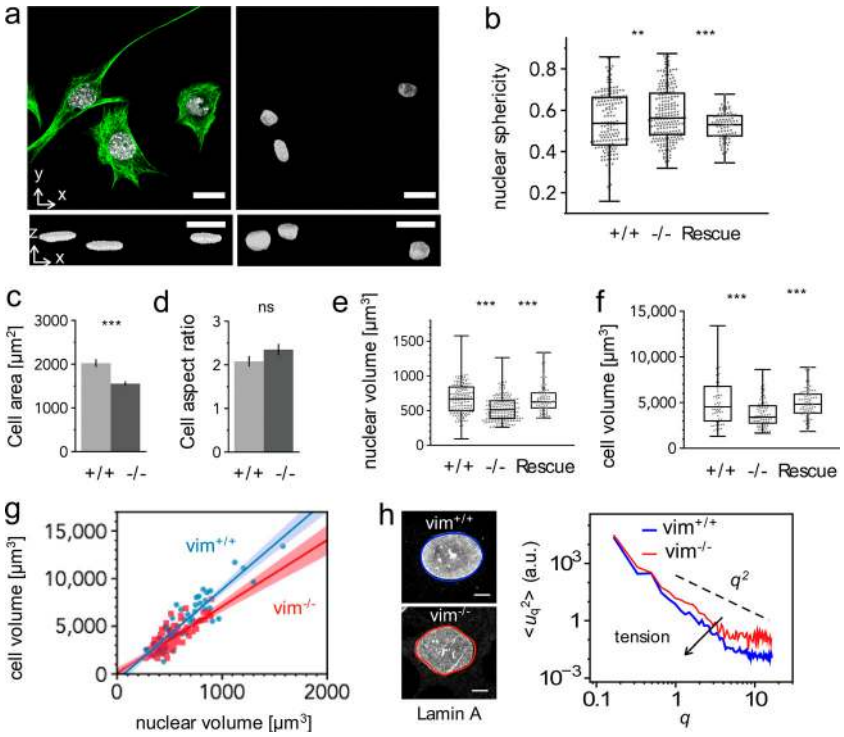

Figure 4. **VIF nuclear cage impacts nuclear shape and volume. (a)** Confocal immunofluorescence images of the VIF network in cells fixed and stained with anti-vimentin (top, green) and nucleus (DAPI, white); and in orthogonal view for the 3D renderings of the nuclei of the same cells (bottom) in vim$^{+/+}$ and vim$^{-/-}$ mEFs. Images show loss of vimentin changes nuclear morphology. Scale bar is 20 µm. The nuclei of cells lacking vimentin are rounder and less smooth compared with those in vim$^{+/+}$ mEFs. **(b)** Vim$^{+/+}$ and rescued mEFs have more compressed, elongated nuclear shapes compared with the vim$^{-/-}$ mEFs (n = 83–219 per condition from at least n = 2 independent experiments). **(c)** Vim$^{-/-}$ mEFs have significantly smaller spread areas compared with the vim$^{+/+}$ or rescued mEFs (n = 62–87 per condition from n = 2 independent experiments). **(d)** Vim$^{+/+}$ and vim$^{-/-}$ mEFs are elongated to the same extent as determined by measuring cell aspect ratio (n = 150–200 per condition from n = 4 independent experiments). Data are presented as means ± standard error, as noted in the statistical analysis section. NS, non significant. **(e and f)** Lack of vimentin decreases nuclear (e; n = 83–219 per condition from at least n = 2 independent experiments) and cell volume (f; n = 62–87 per condition from n = 2 independent experiments). The lower and upper parts of the box represent the 25th and 75th percentiles. The ends of the notch indicate 1.57 times the interquartile range divided by the square root of the number of samples. The whiskers indicate the range of the circular variance up to 1.5 times the interquartile range away from the quartiles. **(g)** Cell volume linearly correlates with nuclear volume but with different slopes ($P < 0.035$) for vim$^{+/+}$ (9.1) and vim$^{-/-}$ mEFs (7.2); the shaded regions correspond to 95% confidence levels based on linear regression analysis. **(h)** Quantification of nuclear shape by determinations using Fourier amplitudes, $u(q)$ (n = 40–43) following staining for immunofluorescence with anti-nuclear lamin A to to trace nuclear contour in vim$^{+/+}$ and vim$^{-/-}$ mEFs. The normalized amplitude decreases as q^2 with a prefactor based on undulated membrane theory that is inversely proportional to the nuclear stress (n = 25 cells per condition from n = 2 independent experiments). The shaded blue and red regions of h represent ± 1 SEM for vim$^{+/+}$ and vim$^{-/-}$ cells, respectively. Scale bar is 5 µm.

model that has previously been applied to cell nuclei (Buxboim et al., 2017). According to such a model, the suppression of shape fluctuations in the presence of VIF corresponds to an increase in nuclear tension or stress. These results are consistent with prior studies using SW-13 cells, which showed that in cells without VIF, the nuclear morphology was more folded and less smooth than in cells with VIF (Sarria et al., 1994). Taken together, our data indicate that VIFs can regulate nuclear morphology.

VIFs confer mechanical stability to the nucleus

To assay the mechanical stability of the NE, we imaged the incidence of nuclear rupture in mEFs transfected with GFP coupled to a nuclear localization signal (NLS-GFP). Live-cell imaging confirmed that the NLS-GFP accumulated in the nucleus (Fig. 5, a and c). Therefore the loss of NLS-GFP fluorescence intensity from the nucleus and into the cytoplasm was indicative of NE rupture events (De Vos et al., 2011; Denais et al., 2016; Vargas et al., 2012; Fig. 5, a and c). In a 15-h observation window, ruptures occurred in 8% of vim$^{+/+}$ and 18% of vim$^{-/-}$ mEFs cultured on 2D substrates, respectively (Fig. 5 b).

NE rupture was more common in 3D collagen gels than on 2D substrates (Fig. 5, b and d, $P < 0.01$ for vim$^{+/+}$ and vim$^{-/-}$ mEFs). Cells cultured in collagen gels exhibited more nuclear blebs and ruptures. These were most frequently seen in cells that migrated through a small pore that constricted the nucleus to a diameter of 2–3 µm. After rupture, many nuclei were repaired, presumably by the endosomal sorting complex, and the NLS-GFP was transported back into the nucleus (Denais et al., 2016; Raab et al., 2016). The incidence of NE rupture and repair was more frequent in vim$^{-/-}$ mEFs (Fig. 5, b and d; Videos 1 and 2); specifically, in the 3D collagen gel assays, the percentage of ruptured nuclei in vim$^{-/-}$ mEFs was >70% higher compared with the vim$^{+/+}$ mEFs (Fig. 5 d, $P = 0.03$). Exogenous expression of wild-type vimentin in vim$^{-/-}$ mEFs restored the nuclear rupture rate to that of vim$^{+/+}$ cells in both 2D and 3D assays (Fig. 5, b and d).

VIFs protect against extreme nuclear deformation and damage during migration through small pores

To examine the role of VIF in nuclear deformations induced by 3D cell migration, we seeded cells on rigid filter membranes with different pore sizes and examined their motility through the pores for 15 h (Fig. 6 a). Results from the migration assays show that vim$^{-/-}$ mEFs transit more readily through the pores of all three diameters (3, 5, and 8 µm) compared with the vim$^{+/+}$ cells ($P < 0.01$), and that the expression of vimentin in the vim$^{-/-}$ cells rescues the wild-type migration rates (Fig. 6 a). These results are striking because they differ from those on 2D surfaces, where removal or disruption of the VIF network in fibroblasts reduces motility (Eckes et al., 1998; Helfand et al., 2011).

To compare the role of nuclear size in cell movement through the filters, we compared the migration data (Fig. 6 a) to the size

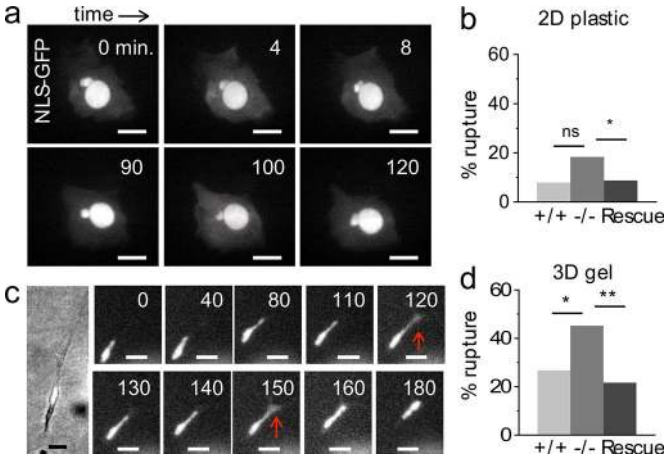

Figure 5. **Loss of VIF increases NE rupture. (a and c)** Sequential images of vim$^{-/-}$ mEF expressing NLS-GFP on 2D tissue culture plastic (a) and in 3D collagen gels (c). Leakage of NLS-GFP signal from the nucleus to the cytoplasm indicates NE rupture. Scale bar is 20 µm. **(b and d)** Fraction of cells with nuclear membrane rupture in 2D (b) and 3D (d) environments (as observed over a 17-h interval). VIFs reduce nuclear membrane ruptures and thereby promote the mechanical stability of the nucleus, particularly in confining 3D gels. The vim$^{-/-}$ phenotype is rescued by the expression of vimentin. Panel a, *n* = 57–63 cells per condition; c, *n* = 38–53 cells; data collected over a minimum of two experiments. *, P < 0.05 based on Fisher's exact test. NS, non significant.

of the nucleus and of the pore (Fig. S3). Here, we calculated the effective nuclear diameter from the shape of a sphere equivalent to the mean volume of the nucleus (Fig. 4 e). Comparing the cell types, we found that the migration rates are significantly increased in vim$^{-/-}$ mEFs compared with vim$^{+/+}$ and rescued mEFs of equivalent nuclear-to-pore-diameter ratios.

Results from immunofluorescence studies show that VIF remains associated with the nucleus after cells translocate through the pores (Fig. 6 b, image shown for a 5-µm pore), suggesting that the VIF network can withstand large strains to protect the nucleus during translocation. In addition, the nuclei in cells that migrated through the membrane had a significantly smaller area compared with those on the top (as determined by manually tracing 2D confocal images of Hoechst-stained nuclei on the membrane). This was the case for both vim$^{+/+}$ and vim$^{-/-}$ mEFs (P < 0.01, Fig. 6 c). This finding indicates that the small pore size of the membrane selects for the passage of cells with smaller nuclei over the 15-h time period used in this assay. This is consistent with the nucleus acting as a rate-limiting step through constricted migration (Friedl and Bröcker, 2000; Davidson et al., 2014; Harada et al., 2014).

Migration through small pores can cause nuclear shape changes that depend on the mechanical properties of both the nucleus and whole cell (Harada et al., 2014). Based on these findings, we determined the aspect ratio of nuclei in the vim$^{+/+}$ and vim$^{-/-}$ mEFs before and after their migration through 3-µm pores (Fig. 6 d). We found that the shape was altered in both vim$^{+/+}$ and vim$^{-/-}$ mEFs after migration (P < 0.01). However, the nuclei were more elongated in vim$^{-/-}$ compared with the vim$^{+/+}$ mEFs (P < 0.001). Fig. 6 d shows sample images of nuclei that have passed through the pores. We observed a fraction of extremely elongated nuclei in the vim$^{-/-}$ mEFs, a phenotype that was not observed in vim$^{+/+}$ cells.

In addition to overall nuclear shape changes, the mEFs exhibit nuclear blebbing after migrating through the 3-µm pores. Immunofluorescence revealed that postmigration nuclear blebs contained mainly dilated lamin A meshworks and little if any lamin B (Fig. 7, a–c). These lamin A–rich blebs have been reported in a variety of cell types under different experimental conditions (Shimi et al., 2008; Denais et al., 2016). Although translocation through the pores increased the fraction of nuclei with blebs in both vim$^{+/+}$ and vim$^{-/-}$ mEFs (Fig. 7 d, P < 0.001), the vim$^{-/-}$ mEFs contained 35% more nuclei with blebs (P = 0.03).

It has also been shown that extreme mechanical deformation of the nucleus during cell migration results in increased DNA damage (Irianto et al., 2017; Bennett et al., 2017), and that nuclear ruptures are related to the sustained loss of DNA damage repair factors (Denais et al., 2016; Raab et al., 2016). Therefore, we determined whether loss of VIF is also associated with increased DNA damage during constricted migration (Fig. 7, e and f). DNA damage repair was assayed by immunostaining for γ-H2AX, a marker of double-strand DNA breaks (Nakamura et al., 2010). From the immunofluorescence images, we determined the average number of γ-H2AX foci per nucleus for vim$^{+/+}$ and vim$^{-/-}$ mEFs before and after migration through 3-µm pores (15 h). The results show a 50% increase in migration-induced DNA damage repair foci in vim$^{-/-}$ mEFs (P < 0.001) compared with the vim$^{+/+}$ mEFs. Qualitatively similar results were found using the mean γ-H2AX intensity signal (Fig. S4). This result is consistent with the increased NE rupture data shown in Fig. 5.

There is abundant evidence that the mechanical integrity of the nucleus, or even the whole cell, depends on the expression levels of nuclear lamin A which, along with the B type lamins, forms the main structural component of the nuclear lamina underlying the NE (Lammerding et al., 2006; Stephens et al., 2017; Swift et al., 2013). We therefore determined the lamin isoform expression levels in vim$^{+/+}$ and vim$^{-/-}$ mEFs by quantitative immunoblotting. Fig. 7 g shows that vim$^{+/+}$ and vim$^{-/-}$ mEFs have indistinguishable amounts of lamins A, B1/2, and C, verifying that lamin isoform expression levels are not altered in vim$^{-/-}$ mEFs. Thus, the changes detected in our experiments reflect the role of VIFs in nuclear mechanics, independent of effects from nuclear lamins.

Vimentin-deficient cells have compromised perinuclear mechanics

Previous studies have shown that vim$^{-/-}$ mEFs have compromised cortical and cytoplasmic stiffness in peripheral regions away from the cell nucleus (Mendez et al., 2014; Vahabikashi et al., 2019). Here, we measured the cytoplasmic stiffness of the cells immediately above the nucleus using atomic force microscopy (AFM; Fig. 8, a and b). The AFM measurements with large AFM round tips show that the apparent Young's modulus (E) over the nucleus of vim$^{-/-}$ mEFs (0.34 ± 0.02 kPa) is reduced by >20% (P < 0.003) compared with the vim$^{+/+}$ mEFs (0.44 ± 0.02 kPa). This mechanical phenotype is reversed in the rescued

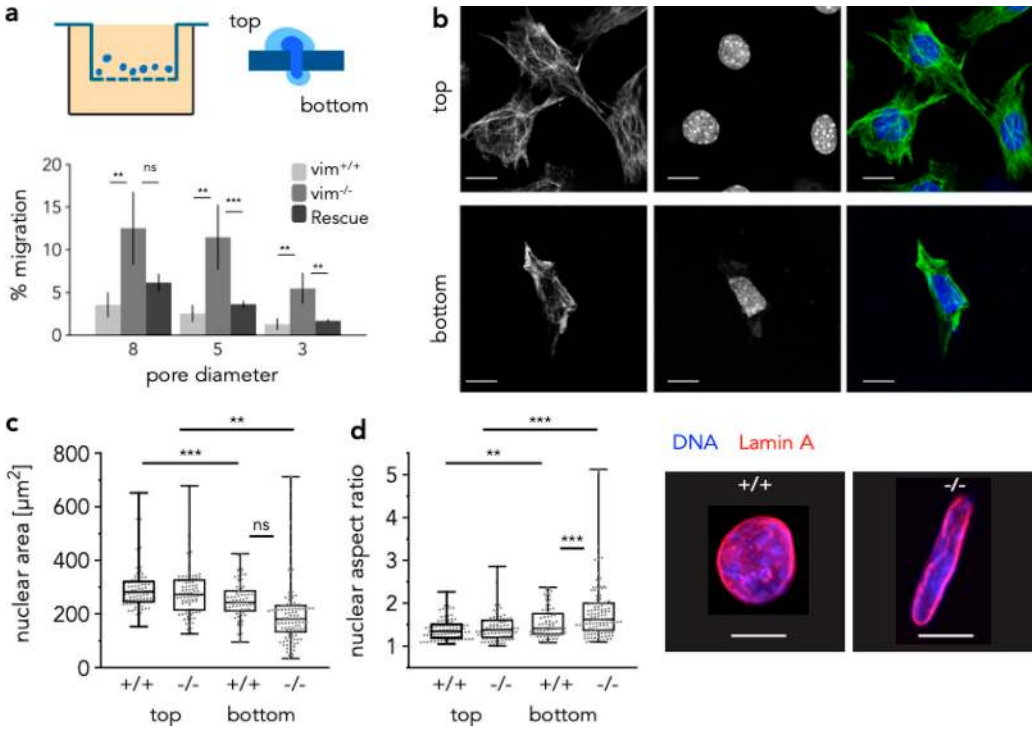

Figure 6. **VIFs hinder migration through small pores but limit nuclear deformation.** Cells are seeded on Transwell membranes and allowed to migrate through pores in the membrane (see schematic). **(a)** Loss of vimentin increases migration through membranes of varying pore sizes, and normal cell motility is restored upon vimentin reexpression (n = 50–150 per condition from n = 2 independent experiments). Data are presented as means ± standard error, as noted in the statistical analysis section. **(b)** Images of vim$^{+/+}$ cells fixed and stained for vimentin and the nucleus (Hoechst) on the top and bottom of the membrane. Scale bar is 20 µm. **(c)** The membranes select for smaller nuclei, as shown by the decrease in nuclear area for cells on top and bottom of the membrane (n = 70–100 per condition from n = 2 independent experiments). **(d)** Pore migration increases nuclear aspect ratio (n = 70–115 per condition from n = 2 independent experiments). The lower and upper parts of the box represent the 25th and 75th percentiles. The ends of the notch indicate 1.57 times the interquartile range divided by the square root of the number of samples. The whiskers indicate the range of the circular variance up to 1.5 times the interquartile range away from the quartiles. In cells lacking vimentin, nuclei are stretched to a greater extent. Immunostaining shows nuclear morphologies on the bottom of the membrane in vim$^{+/+}$ and vim$^{-/-}$ mEFs. The sample image of the vim$^{-/-}$ nucleus is an example of the exceptionally large deformations seen in cells lacking vimentin. Scale bar is 10 µm. ns, non significant.

mEFs where the Young's modulus over the nucleus (0.47 ± 0.03 kPa) is restored to the vim$^{+/+}$ mEF level (P = 0.45). These results show that the lack of VIF under compressive loads leads to greater cell deformation and, potentially, greater damage to the cell and NE.

VIFs reduce necrosis resulting from large external compressions

VIFs are expressed in cells of tissues that are routinely subjected to mechanical stresses (Ramsingh et al., 2011; Conway et al., 2013; Seireg and Arvikar, 1975). Examples include the retina and fat tissues, which regularly undergo compression and extension, and tumors, which generate solid stress (Nia et al., 2018). Whether or not vimentin protects individual cells from damage due to large strains has yet to be determined. We tested the relationships between vimentin expression, externally applied strains, and cell fate in vitro. To this end, we cultured vim$^{+/+}$ and vim$^{-/-}$ mEFs in 3D collagen gels and subjected the gels to axial compression with a parallel-plate rheometer (Fig. 8 c). Cell death was detected by positive staining with propidium iodide, a marker of ruptured cell membranes and necrosis (Fig. 8 d).

In the absence of external compression (0% strain), both vim$^{+/+}$ and vim$^{-/-}$ mEFs had basal levels of necrotic cell death, presumably resulting from the stresses that the contractile cells themselves apply to the matrix and to restrictions to solute diffusion at the gel boundaries. Necrosis in vim$^{-/-}$ mEFs was 30% higher than vim$^{+/+}$ in uncompressed gels (P = 0.01, Fig. 8 e), which could stem from the motility-induced damage and NE rupture as shown in Fig. 5. This basal level was not due to confinement of the cell-containing gel between the metal plates of the rheometer, because the levels were similar for uncompressed gels in a culture dish and for minimally compressed cells in the rheometer. Large axial compressions of the cell-seeded collagen matrices led to necrosis in both cell types; however, for the large compressive strains (80%), vim$^{-/-}$ cells had a 170% increase in necrosis compared with their vim$^{+/+}$ counterparts (P < 0.001, Fig. 8 e). The compressive stresses to produce these levels of strain ranged from 0 to 100 Pa. Since the Young's moduli of the cell-containing gels at small strains (3× shear modulus ∼90–210 Pa from Fig. S5 by parallel plate rheology) were smaller than that of the cells (∼300–500 Pa from Fig. 8 b by AFM), the individual cell strain was correspondingly lower than that of the whole gel, suggesting that significant necrosis occurs

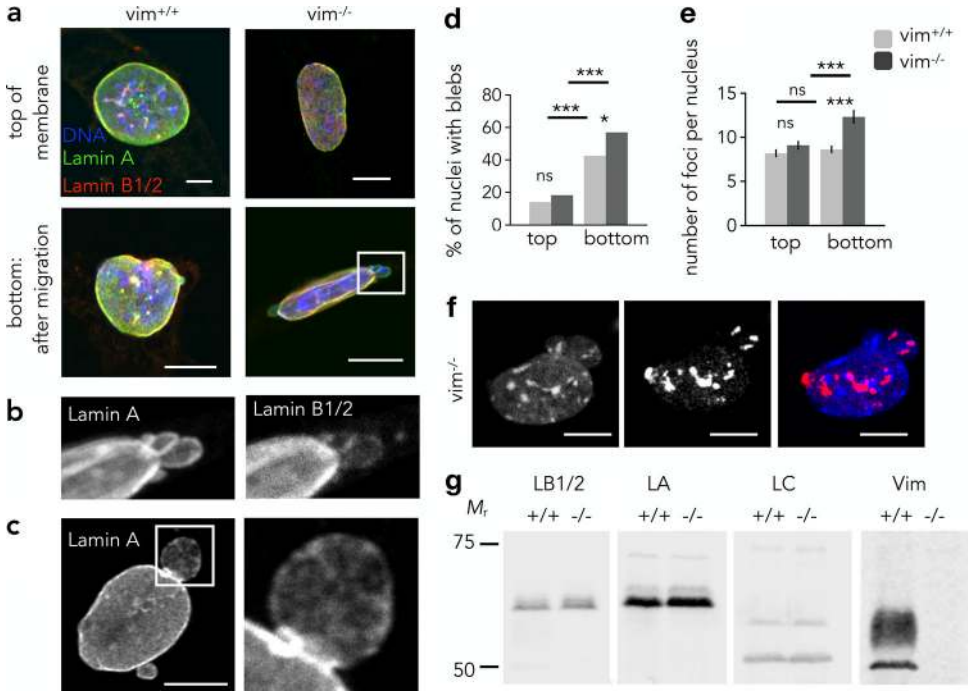

Figure 7. **Loss of vimentin increases nuclear damage but does not alter lamin expression levels. (a–c)** Immunofluorescence images showing lamin A and lamin B1/2 on the top and bottom of membranes with 3 µm pores (a); on the membrane bottom, vim$^{-/-}$ mEFs exhibit nuclear abnormalities such as large nuclear blebs (b), and some blebs exhibit dilated lamin A networks (c). **(d)** Migration through 3-µm pores results in an increased percentage of nuclei with blebs in vim$^{+/+}$ and vim$^{-/-}$ mEFs, but vim$^{-/-}$ mEFs have a significantly higher percentage of migration-induced blebs (n = 70–115 per condition from n = 2 independent experiments). Data are presented as means ± standard error, as noted in the statistical analysis section. **(e and f)** Loss of vimentin increases the number of postmigration DNA double-strand break foci, as determined by immunofluorescence with anti-γH2AX in nuclei after mEFs have migrated to the bottom of membranes with 3 µm pores (n = 70–115 per condition from n = 2 independent experiments). **(g)** Foci appear throughout the nucleus and in protruding blebs. Vim$^{+/+}$ and vim$^{-/-}$ mEFs express equivalent levels of lamin A, B1/2, and C, as shown by quantitative immunoblotting. Scale bars: a, 10 µm; b, 2 µm; c, 10 µm, 2 µm (magnification); f, 10 µm. NS, non significant.

in the vim$^{-/-}$ mEFs under physiologically relevant levels of compressive stress and strain. Overall, these results highlight that VIFs protect the cell from both passive and active deformations that can cause damage and control cell fate.

Discussion

Mechanically induced deformations of the nucleus in cells migrating through small channels can cause NE blebbing, rupture, and DNA damage. To date, these changes have mainly been attributed to regulation by nuclear lamin A, one of the four lamin isoforms belonging to the type V IF protein family (Denais et al., 2016; Irianto et al., 2016, 2017; McGregor et al., 2016; Stephens et al., 2018). The lamins are major filamentous components of the nuclear lamina, which is closely associated with the inner membrane of the NE (Dechat et al., 2010). The role of lamins in nuclear mechanics, especially under conditions of high deformation, is supported to some extent by the strain-stiffening properties of the lamina (Stephens et al., 2017, 2018). Recent studies using cryo-EM tomography have revealed that the lamina is only ∼14 nm thick and that lamin filaments cover ∼50% of the nuclear surface (Turgay et al., 2017). It is unlikely that this very thin layer of lamins at the nuclear surface is sufficient to protect the nuclear contents from the large mechanical stresses that occur as cells move through tight spaces or are compressed by adjacent tissues. It is for this reason that we have undertaken a study of the role of the type III VIFs forming the juxtanuclear cage. This is important, as the strain-stiffening properties of VIFs and their resistance to large deformations have been well documented (Kreplak et al., 2005; Block et al., 2017).

Our results show that in the absence of VIFs, cells migrate more frequently through small spaces. While changes in nuclear volume (Fig. 4 e) could contribute to this effect, the significant increase in motility of vim$^{-/-}$ mEFs (Fig. 6 a) is much stronger than might be expected based only on nuclear volume (Fig. S3). An alternative explanation is that the faster movement of vim$^{-/-}$ mEFs through confining spaces is due to the additional cellular work needed to deform the perinuclear VIF cage in normal cells. Our data are quantitatively consistent with a model of cell migration that treats crossing the channel within the filter as an activate process. It follows that the rates of migration within the channel would be regulated by the requirement to overcome the energy barriers necessary for the successful migration through the channel (Patteson et al., 2018 *Preprint*). Based on this biophysical mechanism, differences in cell migration can be explained predominantly through VIF-mediated changes in cell stiffness (Fig. 8 b; Patteson et al., 2018 *Preprint*). These data suggest that the presence of VIFs protects the nucleus by providing mechanical resistance to the large deformations associated with confined migration. Thus, VIFs function to maintain

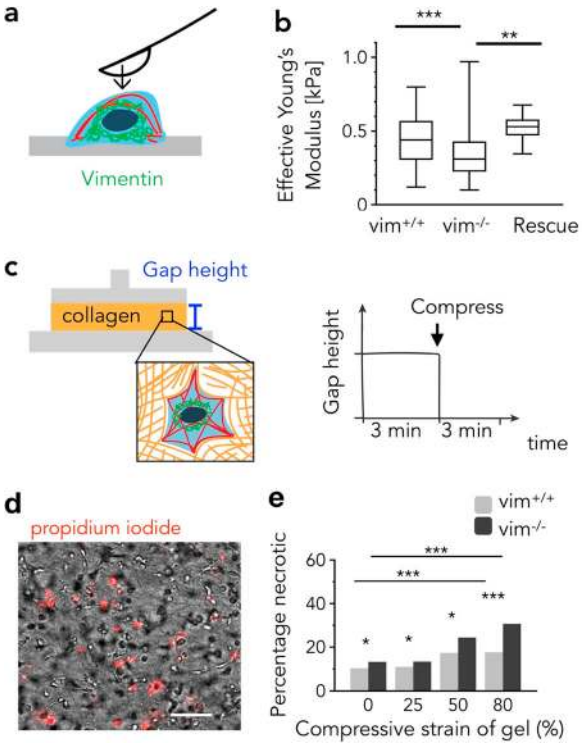

Figure 8. **VIFs provide mechanical resistance and protection against compressive forces. (a and b)** Schematic for the AFM measurements on vim$^{+/+}$, vim$^{-/-}$, and rescued mEFs. The average Young's modulus of the vim$^{-/-}$ mEFs is lower than those of vim$^{+/+}$ mEFs ($P < 0.04$) and rescued mEFs (b; $P < 0.01$; vim$^{+/+}$ [$n = 55$], vim$^{-/-}$ [$n = 80$], and rescued [$n = 20$] from $n = 2$ experiments). The lower and upper parts of the box represent the 25th and 75th percentiles. The ends of the notch indicate 1.57 times the interquartile range divided by the square root of the number of samples. The whiskers indicate the range of the circular variance up to 1.5 times the interquartile range away from the quartiles. **(c)** Schematic image for external compression of a model system of mEFs cultured in 3D collagen gels; the gels are compressed with a parallel plate rheometer at varying degrees of axial strain. **(d)** Cells are stained with propidium iodide to determine the amount of necrotic cell death, as shown for 80% compression. Scale bar is 100 µm. **(e)** Vim$^{-/-}$ mEFs exhibit more necrosis at large strains compared with the vim$^{+/+}$ mEFs, indicating that VIF protect the structural integrity of the cell by resisting large compressive strains ($n = 300–700$ per condition from $n = 2$ independent experiments).

nuclear shape against the imposed deformations, acting like an elastic spring, which is also consistent with the viscoelastic and strain-stiffening properties of VIFs (Janmey et al., 1991). It has been proposed that the ability of IFs to dissipate energy and bear large tensile loads is due to the nonequilibrium unfolding of helices in the monomers comprising the filaments (Block et al., 2018). Recent studies indicate that IFs facilitate stretching at the scale of epithelial sheets, allowing them to accommodate extreme heterogeneous stretching under constant tension (Latorre et al., 2018). Expression of vimentin in vim$^{-/-}$ mEFs resulted in the formation of a VIF network around the nucleus (VIF cage), enhanced perinuclear stiffness, and rescued nuclear shape, DNA stability, and cell migration rates.

Our interpretation of the motility data makes a number of assumptions and simplifications.

The role of regulating actin stress fiber assembly through rho-A (Jiu et al., 2017) and possibly other signaling mechanisms could contribute to differences in motility for vim$^{+/+}$ and vim$^{-/-}$ mEFs. It is also possible that vimentin mediates 3D motility through changes in microtubule and centrosome organization (Shabbir et al., 2014). While no differences in actin or microtubule expression levels have been reported for these two cell lines (Guo et al., 2013; Patteson et al., 2018 *Preprint*), future work should move beyond cytoskeleton studies in 2D by incorporating measures of cytoskeletal assembly dynamics and organization in 3D confining environments, such as microfluidic channels.

Previous studies have demonstrated a role for the actin cytoskeleton in regulating nuclear shape where the typically flat oblate nuclear profile has been attributed to compression forces from the acto-myosin machinery (Kim et al., 2016; Khatau et al., 2009). While the expression levels for actin, myosin, and phosphorylated myosin are similar in vim$^{+/+}$ and vim$^{-/-}$ mEFs (Patteson et al., 2018 *Preprint*), it has been shown that vim$^{-/-}$ mEFs have a significantly softer cortex and are deficient in generating traction forces compared with vim$^{+/+}$ mEFs. In this study, we found that vim$^{-/-}$ mEFs have altered nuclear shapes and are significantly rounder compared with the vim$^{+/+}$ mEFs despite the fact that we found no significant differences in F-actin distribution between the two cell types (Fig. S2). As a result, we propose that the deficiencies in cortical stiffness and contractility of vim$^{-/-}$ mEFs are, to a great extent, responsible for their altered cell spreading and changes in nuclear shape/volume. From these findings, we conclude that the interactions between VIFs and F-actin work synergistically to provide the forces and mechanical requirements for maintaining the profile of the nucleus.

A recent study (Li et al., 2015) showed that nuclear shape is regulated by the moving boundaries of the cell and the extent of cell spreading. Consistent with Li et al. (2015), we found a significant correlation between the sphericity of the nucleus and cell spreading in both vim$^{+/+}$ and vim$^{-/-}$ mEFs. The more spread vim$^{+/+}$ mEFs had relatively flatter nuclei compared with their vim$^{-/-}$ counterparts. We also found significant vimentin dependence for the effect of cell spreading on nuclear shape. In other words, while the effect of cell spreading on nucleus shape is significant in both vim$^{+/+}$ and vim$^{-/-}$ mEFs, we found this effect to be different between the two cell types, rendering vimentin a notable component in regulating nuclear shape. Together, these findings imply that vimentin may regulate nucleus shape and volume through its effect on cell spreading and volume regulation or its interaction with F-actin and regulation of cortex mechanics and cell contractility state.

The nuclear shape fluctuation analysis described in our studies suggests a decrease in nuclear tension in vim$^{-/-}$ mEFs that could also contribute to the nuclear rounding observed in these cells. A potential explanation for the role of juxtanuclear VIF in regulating nuclear shape is its known interactions with F-actin via cytolinkers such as plectin, which also bind VIFs. Alternatively VIFs may regulate nuclear shape by exerting tension on the nucleus through their connections to nesprin-3, a member of the LINC complex, which interacts with both plectin (Wilhelmsen et al., 2005) and F-actin (Fontao et al., 2001). Recent studies indicate that during cell migration through extracellular matrices, the nucleus compartmentalizes the cell and is

pulled toward the leading edge by actomyosin filaments. These latter filaments act through VIFs and nesprin-3 to create the high pressure required for lobopodia formation at the leading edge of locomoting cells (Shulman et al., 2014). Based on our results, we expect that cells subjected to high levels of mechanical stress may enhance vimentin expression to protect the nucleus against large strains but still allow for migration through tissues. In support of this, it has been recently shown that VIFs regulate the mechanical properties of both the cell cortex and subcortical cytoplasm and also the generation of traction forces required for cell motility.

The lower apparent tension of the nucleus of vim$^{-/-}$ cells at rest, inferred from their rounder shape (Fig. 4 a) and higher degree of fluctuation (Fig. 4 f), might appear at odds with the finding that the VIF perinuclear cage protects the nucleus from potentially disruptive stresses. Physically, the explanation lies in the highly nonlinear response of VIF networks to applied stresses. At low stress and strain, VIF networks are soft, and therefore even if they transmit forces exerted by the cortical cytoskeleton when cells adhere to a rigid surface, they effectively average out these forces, preventing the large curvature deformations that can lead to NE rupture (Xia et al., 2018). However, at large deformations, the VIF networks become much stiffer and therefore can take up the stress generated by the cytoskeletal contraction that drives the cell through small spaces, sparing the nucleus from these large, transient stresses. The lower levels of necrosis in cell-embedded collagen gels suggest that the strain stiffening of VIF networks prevents excessive deformations at the level of the nucleus and at the level of stresses that are strong enough to rupture an F-actin network that might lead to cell lysis.

Taken together, our results demonstrate a new role for VIFs in maintaining nuclear shape and mechanical stability. We established that VIFs are involved in mechanisms regulating the shape of the nucleus, and that during migration through small channels, their absence causes nuclei to undergo higher degrees of deformation, blebbing, and DNA damage in response to the compressive forces. Our results provide new insights into the protective role of VIF in cells undergoing large strains, with implications for cell fate, genome expression and integrity, healthy tissue maintenance, development, and disease progression.

Materials and methods

Cell culture

The vim$^{+/+}$ and vim$^{-/-}$ mEFs were derived from vim$^{+/+}$ and vimentin-null mice and immortalized by stable expression of SV40 large T antigen (kindly provided by J. Eriksson, Abo Akademi University, Turku, Finland). Cells were cultured in DMEM with 25 mM Hepes and sodium pyruvate (Life Technologies) supplemented with 10% FBS, 1% penicillin/streptomycin, and nonessential amino acids. All cell cultures were maintained at 37°C and 5% CO_2.

For the reconstitution of vimentin protein expression in vim$^{-/-}$ mEFs, the vimentin cDNA was expressed from pLVX-IRES-neo (Clonetech) by lentiviral transduction. To express the SNAP-vimentin fusion protein, the vimentin cDNA was subcloned into pLVX-IRES-puro (Clontech) with the addition of a SNAP tag (NEB). After selection of the transduced cells with the appropriate antibiotic for 1 wk vimentin expression was assessed by Western blotting using mouse anti-vimentin antibody (Sigma, clone V9, V6630) as described before (Gan et al., 2016).

Immunofluorescence and microscopy

Cells were fixed in either methanol for 10 min at −20°C or 4% PFA in PBS for 30 min, followed by permeabilization in 0.05% Triton X-100 in PBS for 15 min at RT. After fixation, cells were rinsed in PBS and blocked with 1% BSA for 30 min at RT. Fixed cells were stained for 1 h at RT or overnight at 4°C for single- or double-label immunofluorescence with the following primary antibodies: chicken anti-vimentin (1:200, Novus, NB300-223); rabbit anti-Lamin A (#323, Goldman laboratory); and mouse monoclonal anti-Lamin B1/2 (1:1,000, 2B2, Goldman laboratory). DNA damage repair foci were stained with monoclonal mouse anti-γH2AX at 1:500 (EMD Millipore, 05-636) overnight at 4°C. After fixation, cells were washed in PBS at RT and then incubated with the appropriate secondary antibody: goat anti-chicken Alexa Fluor 488 (1:1,000, Invitrogen, A-11039), goat anti-rabbit Alexa Fluor 488 (1:1,000, Thermo Fisher Scientific, A-11008), goat anti-mouse Alexa Fluor 568 (1:1,000, Thermo Fisher Scientific, A-11004), or goat anti-mouse Alexa Fluor 488 (1:500, Thermo Fisher Scientific, A-11029). Cells were washed and stained with Hoechst 33342 (Molecular Probes, H-1399) and, in some cases, Alexa Fluor 647 phalloidin (Molecular Probes, 8940S) for 1 h according to the manufacturer's instructions. For the NLS-GFP experiments (Fig. 4) and necrosis assays (Fig. 6), cells were imaged with an inverted Leica DMIRE2 microscope equipped with either a 10×/0.3-NA or a 40×/0.55-NA air objective. For the Transwell migration assays (Figs. 5 and 6), cells were imaged with an inverted Leica TCS SP8 confocal microscope equipped with a 40×/1.2-NA water objective. For the VIF cage/F-actin visualization, 3D measurements, and sphericity analysis experiments, a Zeiss 510 LSM inverted confocal microscope with a 63× (oil immersion, NA 1.4) objective lens and excitation sources of Ar (458, 488, and 514 nm), HeNe (543 nm), and HeNe (633 nm) were used to create confocal stacks (Carl Zeiss). For SIM images, the coverslips containing fix-immunostained cells were mounted on slides using Prolong Diamond (Thermo Fisher Scientific). 3D-SIM was performed with a Nikon Structured Illumination Super Resolution Microscope System (Nikon N-SIM) with an oil-immersion objective lens CFI SR (Apochromat TIRF 100×, 1.49 NA; Nikon).

Image analysis methods

Matlab was used to load the raw images using BioFormats and calculate maximum-intensity projections. The nucleus was segmented by applying smoothing with a Gaussian kernel with an SD of 4 pixels. The method of Otsu (1979) was used to automatically calculate a threshold based on the smoothed image. The threshold was then used to binarize the smooth image to provide a segmentation of the nuclei from the pixels above the threshold. The nuclei were then subjected to connected component analysis, and the centroids and areas were calculated.

Nuclei segmentations were accepted if the calculated area was ≥89 μm². A Euclidean distance map relative to the segmented nuclei was calculated, and a watershed transformation was done to partition the image into regions closest to each nucleus. Within each region, pixels were discretized into 1-μm increments away from the boundaries of the nucleus. Within each 1-μm-distance increment, a Gaussian kernel as a function angle with a SD of 7.2° was used as a kernel to calculate a moving average of the intensity profile around the nucleus. 51 equidistant angular samples were measured and interpolated using a zero padded Fourier transform at 1° increments to produce the smooth angular histograms shown. The function "circ r" was used from the CircStats Toolbox for Matlab (Berens, 2009) to calculate the resultant vector lengths based on the 51 angular samples. The circular variance, S, was calculated from the resultant vector lengths, R, by the equation $S = 1 - R$. The distribution of variances was first subjected to a one-sample Kolmogorov–Smirnov test where the null hypothesis that the samples came from normal distributions was rejected. The samples were then subjected to the Wilcoxon rank sum test using Matlab to test the null hypothesis that the samples came from continuous distributions with equal medians.

Immunoblotting

Cell lysates in 1× SDS sample buffer containing equal numbers of vim$^{+/+}$ and vim$^{-/-}$ mEFs were separated in triplicate by SDS-PAGE and electrophoretically transferred to nitrocellulose. After blocking in 5% nonfat dry milk in PBS with 0.1% Tween 20, the blots were probed with a 1:4,000 dilution of chicken anti-vimentin antibody (in blocking buffer overnight at 4°C). For immunoblotting of lamins in mEFs, lysates from equal numbers of vim$^{+/+}$ and vim$^{-/-}$ mEFs were separated by SDS-PAGE and transferred to nitrocellulose. Separate blots for each lamin were probed with either rabbit polyclonal anti-LA 1:500, 323; rabbit polyclonal anti-LC 1:500, 321; or mouse monoclonal antibody 2B2 for LB1/LB2. After washing three times for 5 min each in PBS with 0.1% Tween 20, the blots were probed with a 1:15,000 dilution of IRDye 800CW donkey anti-chicken IgG, donkey anti-rabbit, or donkey anti-mouse (LI-COR) in 5% nonfat dry milk in PBS with 0.2% Tween 20 for 45 min at RT. After washing three times for 5 min each in PBS with 0.2% Tween 20, the blot was allowed to air dry in the dark. Imaging was performed on a LI-COR Odyssey Fc, and the resulting image was analyzed using LI-COR Image Studio v5.2. The amount of vimentin in each type of cell is expressed as an average of the three replicates.

3D collagen gel preparation and imaging

Collagen gels (2 mg/ml) were prepared with final concentrations of 400,000 cells/ml. The procedure involved removing growing cells from Petri dishes by trypsin followed by pelleting and counting cells in culture medium (DMEM with 10% FBS, 10 mM NaOH, and 2 mg/ml collagen type I; Corning, 354236). Reagents were kept cold on ice while mixing. 1 ml of this mixture was added to 20-mm dishes and maintained at 37°C and 5% CO_2. Experiments were conducted 24 h after seeding the cells in the gel. The nuclei of vim$^{+/+}$ and vim$^{-/-}$ mEFs were fluorescently labeled by transient transfection with pEGFP-C1-NLS, 48 h before seeding in collagen gels. Cell nuclei were imaged at 10-min increments for 18 h by using wide-field fluorescence with a 10×, 0.3-NA objective.

Fourier transformation

To quantify the structural features of nuclei, we traced the contour, $r(\theta)$, of lamin A–stained nuclei. The images were captured from methanol-fixed cells with a Leica TCS SP8 confocal microscope equipped with a 40× water-immersion lens. Each nucleus was traced manually, and its contour was interpolated from 0 to 2π by 200 points. Next, the shape fluctuations were calculated as $u(\theta) = r(\theta) - r_0$, where r_0 is the average radius. Next, the wave number–dependent Fourier modes of the fluctuations, u_q, were obtained as

$$u_q = \frac{1}{2\pi}\int_0^{2\pi} u(\theta)e^{-iq\theta}d\theta.$$

Here, the wave number q varies from ∼0.15 to 30, which corresponds to 0.01π and 2π. The average shape fluctuations were quantified by computing the Fourier mode magnitude square u_q^2 and averaging over 25 cells from two experiments.

Transwell migration assays

Vim$^{+/+}$ and vim$^{-/-}$ mEFs were seeded at subconfluent concentrations (10,000–20,000 cells/cm²) on polycarbonate Transwell membranes with pore diameters of 3, 5, or 8 μm (Corning). Membranes were precoated with collagen I (50 μg/ml). mEF-seeded filters were maintained at 37°C and 5% CO_2 for 18 h. The cells were then gently removed from either the top or bottom of the membrane with a cotton swab, and the membrane with the remaining cells was immediately fixed with either PFA or methanol, stained, and imaged. Nuclear morphologies were determined by Hoechst staining and manually tracing nuclei using ImageJ (National Institutes of Health). Binucleated cells and nuclei <75 μm², which were likely to be micronuclei, were excluded. Experiments were conducted a minimum of two times, and a total of 90–100 cells were imaged and analyzed on the top of the membrane and 65–80 cells on the bottom for both the vim$^{+/+}$ and vim$^{-/-}$ mEFs. To determine the rate of migration through the pores, the cells were stained with crystal violet after fixation and imaged at multiple locations across the membrane with a 10× objective. Cells were manually counted in 800 × 800-μm² fields of view (12–30 locations per condition). The percentage of cells that crossed the membrane was determined by the ratio of the number of cells on the bottom of the membrane and the sum of cells on the filter top and bottom.

Axial compression of cell-embedded collagen matrices

Collagen gels embedded with either vim$^{+/+}$ or vim$^{-/-}$ mEFs (400,000 cells/ml; see above) were prepared in culture dishes such that the dimensions of the gel were 20-mm in diameter and 1-mm in height. After 24 h, the gels were deposited onto a Kinexus rheometer (Malvern) equipped with a 20-mm circular parallel plate geometry and Peltier plate that maintains the sample temperature at 37°C. The upper plate was lowered to contact the gel. Cell culture medium was added around the sample to prevent drying and allow free fluid flow. The gel was

allowed to relax for a minimum of 3 min between the plates and then subjected to a step compression of 25%, 50%, or 80% strain, which was held for 3 min to allow for axial stresses to relax to steady state. The plate was raised, and the gel was transferred to a culture dish with cell culture medium. Cell fate was determined in 3D collagen gels by staining with propidium iodide (Invitrogen, V13241) according to the manufacturer's instructions. The cell membrane is impermeable to propidium iodide, and positive staining indicates rupture of the cell membrane and necrotic cell death. Cells were imaged at multiple locations throughout the gel with a 10× objective and manually counted in 800 × 800-μm^2 areas (five to eight locations per condition). Experiments were conducted a minimum of two times, yielding 300–700 cells per condition.

Statistical analysis

Data are presented as mean values ± SEM. Each experiment was performed a minimum of two times unless otherwise stated. The unpaired, two-tailed Student's *t* test at the 95% confidence interval was used to determine statistical significance. *, P ≤ 0.05; **, P < 0.01; ***, P < 0.001; NS, P > 0.05. The Fisher's exact test was used to confirm statistical significance between the proportion of blebbed and ruptured nuclei (Fig. 5) and the proportion of necrotic cells (Fig. 8 e) in vim$^{+/+}$ and vim$^{-/-}$ mEFs. Multiple linear regression for nucleus shape (sphericity) as a function of cell spreading, vimentin, and the relationship between vimentin and cell spreading was done as

$$\text{Sphericity} = \alpha + \beta*[\text{cell spreading}] + \gamma*[\text{vimentin}] + \delta*[\text{cell spreading}]*[\text{vimentin}].$$

3D measurements and sphericity analysis

Confocal Z-stacks (200-nm optical sections) of the nucleus from vim$^{+/+}$ (n = 174), vim$^{-/-}$ (n = 219), and rescued (n = 83) mEFs were imported into Imaris v9.2 software to generate 3D renderings as described previously (Mulholland et al., 2006). The same approach was used to generate 3D renderings of the cell for vim$^{+/+}$ (n = 62), vim$^{-/-}$ (n = 87), and rescued (n = 76) mEFs. Alexa Fluor 647 phalloidin and lamin A staining were used to demarcate the boundaries of the cell and the nucleus. Cell volume, nucleus volume, and nucleus surface area were calculated using the 3D renderings. Nuclear sphericity is defined as

$$\frac{\pi^{1/3}(6V^{2/3})}{A},$$

where V is the nuclear volume and A is the surface area. A value of 1 corresponds to a sphere, with nonspherical shapes <1. When determining the slope of the cell-versus-nuclear volume in Fig. 3 e, cells that corresponded to 2 SDs away from the linear regression analysis (<5% of the cells) were defined as outliers and excluded from the analysis.

AFM

AFM measurements were made using a BioScope Resolve (Bruker) coupled to an inverted fluorescence microscope with 10× (NA 0.3) and 20× (NA 0.8) objective lenses (Carl Zeiss). Rounded AFM probes (10-μm spheres mounted on silicon nitride cantilevers with a nominal spring constant of 0.01 N/m; Novascan Technologies) were used. Indentation depths were kept <500 nm to avoid any substrate effect (Rico et al., 2005), and measurements were made above the cell nucleus. Young's modulus was determined using a modified Hertzian analysis (Rico et al., 2005; Vahabikashi et al., 2019). AFM measurements were made on vim$^{+/+}$ (n = 55), vim$^{-/-}$ (n = 80), and rescued (n = 20) mEFs grown on glass coverslips in culture medium containing 10% FBS. A minimum of 20 measurements were made for each cell type.

Online supplemental material

Fig. S1 shows that the level of vimentin expression in rescued mEFs is similar to that of the vim$^{+/+}$ mEFs. Fig. S2 shows that cell spreading area is larger in vim$^{+/+}$ mEFS compared with vim$^{-/-}$; it also represents the similarity of F-actin and stress fiber distribution below and above the nucleus in vim$^{+/+}$ and vim$^{-/-}$ mEFs. Fig. S3 shows that regardless of nuclear/pore diameter ratio, vim$^{-/-}$ mEFs always migrate at higher percentages compared with vim$^{+/+}$ and rescued cells. Fig. S4 shows that vim$^{-/-}$ mEFs experience significant increases in DNA damage levels after migration through Transwell membranes with 3-μm pores, whereas such an effect is absent in the vim$^{+/+}$ mEFs. Fig. S5 shows the shear modulus of collagen gels embedded with either vim$^{+/+}$ or vim$^{-/-}$ mEFs.

Acknowledgments

We thank Dennis Discher and Manu Tewari for help with plasmid amplification. We are grateful to Dr. Christoph Burckhardt and Joseph Chi in the Danuser laboratory at University of Texas Southwestern Medical Center for developing the rescue vim$^{-/-}$ mEF cell line and providing it for our studies.

This work was supported by the National Institutes of Health, National Institute of General Medical Sciences P01 GM096971 awarded to R.D. Goldman and P.A. Janmey. A. Vahabikashhi is supported by an National Cancer Institute training fellowship (T32 CA080621-15).

The authors declare no competing financial interests.

Author contributions:. A.E. Patteson designed, performed, and analyzed experiments involving nuclear membrane rupture, collagen gels, and constricted pore migration. A. Vahabikashi designed and carried out the nuclear shape and volume measurements, and A. Vahabikashi and K. Pogoda contributed to the AFM experiments and analyses. K. Mandal contributed to experiments involving nuclear membrane rupture with rescue cells. M. Kittisopikul designed and performed quantification of vimentin distribution in the perinuclear region. S.A. Adam provided the constructs used for all analyses and carried out the immunoblotting assays. A. Goldman and S. Sivagurunathan did the SIM imaging. A.E. Patteson, A. Vahabikashi, S.A. Adam, R. Goldman, and P.A. Janmey contributed to project design and manuscript preparation.

Submitted: 1 March 2019
Revised: 12 August 2019
Accepted: 18 September 2019

References

Bennett, R.R., C.R. Pfeifer, J. Irianto, Y. Xia, D.E. Discher, and A.J. Liu. 2017. Elastic-Fluid Model for DNA Damage and Mutation from Nuclear Fluid Segregation Due to Cell Migration. *Biophys. J.* 112:2271–2279. https://doi.org/10.1016/j.bpj.2017.04.037

Berens, P. 2009. CircStat: A MATLAB Toolbox for Circular Statistics. *J. Stat. Softw.* 31:1–21. https://doi.org/10.18637/jss.v031.i10

Block, J., H. Witt, A. Candelli, E.J.G. Peterman, G.J.L. Wuite, A. Janshoff, and S. Köster. 2017. Nonlinear Loading-Rate-Dependent Force Response of Individual Vimentin Intermediate Filaments to Applied Strain. *Phys. Rev. Lett.* 118:048101–048105.

Block, J., H. Witt, A. Candelli, J.C. Danes, E.J.G. Peterman, G.J.L. Wuite, A. Janshoff, and S. Köster. 2018. Viscoelastic properties of vimentin originate from nonequilibrium conformational changes. *Sci. Adv.* 4:eaat1161.

Broers, J.L.V., E.A.G. Peeters, H.J.H. Kuijpers, J. Endert, C.V.C. Bouten, C.W.J. Oomens, F.P.T. Baaijens, and F.C.S. Ramaekers. 2004. Decreased mechanical stiffness in LMNA−/− cells is caused by defective nucleocytoskeletal integrity: implications for the development of laminopathies. *Hum. Mol. Genet.* 13:2567–2580. https://doi.org/10.1093/hmg/ddh295

Burke, B., and C.L. Stewart. 2014. Functional Architecture of the Cell's Nucleus in Development, Aging, and Disease. *Curr. Top Dev. Biol.* 109:1–52.

Buxboim, A., J. Irianto, J. Swift, A. Athirasala, J.-W. Shin, F. Rehfeldt, and D.E. Discher. 2017. Coordinated increase of nuclear tension and lamin-A with matrix stiffness outcompetes lamin-B receptor that favors soft tissue phenotypes. *Mol. Biol. Cell.* 28:3333–3348. https://doi.org/10.1091/mbc.e17-06-0393

Conway, D.E., M.T. Breckenridge, E. Hinde, E. Gratton, C.S. Chen, and M.A. Schwartz. 2013. Fluid shear stress on endothelial cells modulates mechanical tension across VE-cadherin and PECAM-1. *Curr. Biol.* 23:1024–1030. https://doi.org/10.1016/j.cub.2013.04.049

Dahl, K.N., A.J. Engler, J.D. Pajerowski, and D.E. Discher. 2005. Power-law rheology of isolated nuclei with deformation mapping of nuclear substructures. *Biophys. J.* 89:2855–2864. https://doi.org/10.1529/biophysj.105.062554

Davidson, P.M., C. Denais, M.C. Bakshi, and J. Lammerding. 2014. Nuclear deformability constitutes a rate-limiting step during cell migration in 3-D environments. *Cell. Mol. Bioeng.* 7:293–306. https://doi.org/10.1007/s12195-014-0342-y

De Vos, W.H., F. Houben, M. Kamps, A. Malhas, F. Verheyen, J. Cox, E.M.M. Manders, V.L.R.M. Verstraeten, M.A.M. van Steensel, C.L.M. Marcelis, et al. 2011. Repetitive disruptions of the nuclear envelope invoke temporary loss of cellular compartmentalization in laminopathies. *Hum. Mol. Genet.* 20:4175–4186. https://doi.org/10.1093/hmg/ddr344

Dechat, T., S.A. Adam, P. Taimen, T. Shimi, and R.D. Goldman. 2010. Nuclear lamins. *Cold Spring Harb. Perspect. Biol.* 2:a000547. https://doi.org/10.1101/cshperspect.a000547

Denais, C.M., R.M. Gilbert, P. Isermann, A.L. McGregor, M. te Lindert, B. Weigelin, P.M. Davidson, P. Friedl, K. Wolf, and J. Lammerding. 2016. Nuclear envelope rupture and repair during cancer cell migration. *Science.* 352:353–358. https://doi.org/10.1126/science.aad7297

Dupin, I., Y. Sakamoto, and S. Etienne-Manneville. 2011. Cytoplasmic intermediate filaments mediate actin-driven positioning of the nucleus. *J. Cell Sci.* 124:865–872. https://doi.org/10.1242/jcs.076356

Eckes, B., D. Dogic, E. Colucci-Guyon, N. Wang, A. Maniotis, D. Ingber, A. Merckling, F. Langa, M. Aumailley, A. Delouvée, et al. 1998. Impaired mechanical stability, migration and contractile capacity in vimentin-deficient fibroblasts. *J. Cell Sci.* 111:1897–1907.

Fontao, L., D. Geerts, I. Kuikman, J. Koster, D. Kramer, and A. Sonnenberg. 2001. The interaction of plectin with actin: evidence for cross-linking of actin filaments by dimerization of the actin-binding domain of plectin. *J. Cell Sci.* 114:2065–2076.

Friedl, P., and E.B. Bröcker. 2000. T cell migration in three-dimensional extracellular matrix: guidance by polarity and sensations. *Dev. Immunol.* 7:249–266. https://doi.org/10.1155/2000/56473

Gan, Z., L. Ding, C.J. Burckhardt, J. Lowery, A. Zaritsky, K. Sitterley, A. Mota, N. Costigliola, C.G. Starker, D.F. Voytas, et al. 2016. Vimentin Intermediate Filaments Template Microtubule Networks to Enhance Persistence in Cell Polarity and Directed Migration. *Cell Syst.* 3:252–263.e8. https://doi.org/10.1016/j.cels.2016.08.007

Guo, M., A.J. Ehrlicher, S. Mahammad, H. Fabich, M.H. Jensen, J.R. Moore, J.J. Fredberg, R.D. Goldman, and D.A. Weitz. 2013. The role of vimentin intermediate filaments in cortical and cytoplasmic mechanics. *Biophys. J.* 105:1562–1568. https://doi.org/10.1016/j.bpj.2013.08.037

Harada, T., J. Swift, J. Irianto, J.-W. Shin, K.R. Spinler, A. Athirasala, R. Diegmiller, P.C.D.P. Dingal, I.L. Ivanovska, and D.E. Discher. 2014. Nuclear lamin stiffness is a barrier to 3D migration, but softness can limit survival. *J. Cell Biol.* 204:669–682. https://doi.org/10.1083/jcb.201308029

Hay, E.D. 2005. The mesenchymal cell, its role in the embryo, and the remarkable signaling mechanisms that create it. *Dev. Dyn.* 233:706–720. https://doi.org/10.1002/dvdy.20345

Helfand, B.T., M.G. Mendez, S.N.P. Murthy, D.K. Shumaker, B. Grin, S. Mahammad, U. Aebi, T. Wedig, Y.I. Wu, K.M. Hahn, et al. 2011. Vimentin organization modulates the formation of lamellipodia. *Mol. Biol. Cell.* 22:1274–1289. https://doi.org/10.1091/mbc.e10-08-0699

Herrmann, H., and U. Aebi. 2016. Intermediate Filaments: Structure and Assembly. *Cold Spring Harb. Perspect. Biol.* 8:a018242-24. https://doi.org/10.1101/cshperspect.a018242

Irianto, J., C.R. Pfeifer, R.R. Bennett, Y. Xia, I.L. Ivanovska, A.J. Liu, R.A. Greenberg, and D.E. Discher. 2016. Nuclear constriction segregates mobile nuclear proteins away from chromatin. *Mol. Biol. Cell.* 27:4011–4020. https://doi.org/10.1091/mbc.E16-06-0428

Irianto, J., Y. Xia, C.R. Pfeifer, A. Athirasala, J. Ji, C. Alvey, M. Tewari, R.R. Bennett, S.M. Harding, A.J. Liu, et al. 2017. DNA Damage Follows Repair Factor Depletion and Portends Genome Variation in Cancer Cells after Pore Migration. *Curr. Biol.* 27:210–223. https://doi.org/10.1016/j.cub.2016.11.049

Janmey, P.A., U. Euteneuer, P. Traub, and M. Schliwa. 1991. Viscoelastic properties of vimentin compared with other filamentous biopolymer networks. *J. Cell Biol.* 113:155–160. https://doi.org/10.1083/jcb.113.1.155

Jiu, Y., J. Peränen, N. Schaible, F. Cheng, J.E. Eriksson, R. Krishnan, and P. Lappalainen. 2017. Vimentin intermediate filaments control actin stress fiber assembly through GEF-H1 and RhoA. *J. Cell Sci.* 130:892–902. https://doi.org/10.1242/jcs.196881

Ketema, M., M. Kreft, P. Secades, H. Janssen, and A. Sonnenberg. 2013. Nesprin-3 connects plectin and vimentin to the nuclear envelope of Sertoli cells but is not required for Sertoli cell function in spermatogenesis. *Mol. Biol. Cell.* 24:2454–2466. https://doi.org/10.1091/mbc.e13-02-0100

Khatau, S.B., C.M. Hale, P.J. Stewart-Hutchinson, M.S. Patel, C.L. Stewart, P.C. Searson, D. Hodzic, and D. Wirtz. 2009. A perinuclear actin cap regulates nuclear shape. *Proc. Natl. Acad. Sci. USA.* 106:19017–19022. https://doi.org/10.1073/pnas.0908686106

Kim, D.-H., B. Li, F. Si, J.M. Phillip, D. Wirtz, and S.X. Sun. 2016. Volume regulation and shape bifurcation in the cell nucleus. *J. Cell Sci.* 129:457. https://doi.org/10.1242/jcs.185173

Kreplak, L., H. Bär, J.F. Leterrier, H. Herrmann, and U. Aebi. 2005. Exploring the mechanical behavior of single intermediate filaments. *J. Mol. Biol.* 354:569–577. https://doi.org/10.1016/j.jmb.2005.09.092

Lammerding, J., L.G. Fong, J.Y. Ji, K. Reue, C.L. Stewart, S.G. Young, and R.T. Lee. 2006. Lamins A and C but not lamin B1 regulate nuclear mechanics. *J. Biol. Chem.* 281:25768–25780. https://doi.org/10.1074/jbc.M513511200

Latorre, E., S. Kale, L. Casares, M. Gómez-González, M. Uroz, L. Valon, R.V. Nair, E. Garreta, N. Montserrat, A. Del Campo, et al. 2018. Active superelasticity in three-dimensional epithelia of controlled shape. *Nature.* 563:203–208. https://doi.org/10.1038/s41586-018-0671-4

Lele, T.P., R.B. Dickinson, and G.G. Gundersen. 2018. Mechanical principles of nuclear shaping and positioning. *J. Cell Biol.* 217:3330–3342. https://doi.org/10.1083/jcb.201804052

Li, Y., D. Lovett, Q. Zhang, S. Neelam, R.A. Kuchibhotla, R. Zhu, G.G. Gundersen, T.P. Lele, and R.B. Dickinson. 2015. Moving Cell Boundaries Drive Nuclear Shaping during Cell Spreading. *Biophys. J.* 109:670–686. https://doi.org/10.1016/j.bpj.2015.07.006

Lodish, H., A. Berk, S.L. Zipursky, P. Matsudaira, D. Baltimore, and J. Darnell. 2000. *Molecular Cell Biology*. Fourth edition. W. H. Freeman, New York. 973 pp.

Lowery, J., E.R. Kuczmarski, H. Herrmann, and R.D. Goldman. 2015. Intermediate Filaments Play a Pivotal Role in Regulating Cell Architecture and Function. *J. Biol. Chem.* 290:17145–17153. https://doi.org/10.1074/jbc.R115.640359

Maniotis, A.J., C.S. Chen, and D.E. Ingber. 1997. Demonstration of mechanical connections between integrins, cytoskeletal filaments, and nucleoplasm that stabilize nuclear structure. *Proc. Natl. Acad. Sci. USA.* 94:849–854. https://doi.org/10.1073/pnas.94.3.849

McGregor, A.L., C.-R. Hsia, and J. Lammerding. 2016. Squish and squeeze-the nucleus as a physical barrier during migration in confined environments. *Curr. Opin. Cell Biol.* 40:32–40. https://doi.org/10.1016/j.ceb.2016.01.011

Mendez, M.G., S. Kojima, and R.D. Goldman. 2010. Vimentin induces changes in cell shape, motility, and adhesion during the epithelial to mesenchymal transition. *FASEB J.* 24:1838–1851. https://doi.org/10.1096/fj.09-151639

Mendez, M.G., D. Restle, and P.A. Janmey. 2014. Vimentin enhances cell elastic behavior and protects against compressive stress. *Biophys. J.* 107: 314–323. https://doi.org/10.1016/j.bpj.2014.04.050

Mulholland, W.J., E.A.H. Arbuthnott, B.J. Bellhouse, J.F. Cornhill, J.M. Austyn, M.A.F. Kendall, Z. Cui, and U.K. Tirlapur. 2006. Multiphoton high-resolution 3D imaging of Langerhans cells and keratinocytes in the mouse skin model adopted for epidermal powdered immunization. *J. Invest. Dermatol.* 126:1541–1548. https://doi.org/10.1038/sj.jid.5700290

Murray, M.E., M.G. Mendez, and P.A. Janmey. 2014. Substrate stiffness regulates solubility of cellular vimentin. *Mol. Biol. Cell.* 25:87–94. https://doi.org/10.1091/mbc.e13-06-0326

Nakamura, A.J., V.A. Rao, Y. Pommier, and W.M. Bonner. 2010. The complexity of phosphorylated H2AX foci formation and DNA repair assembly at DNA double-strand breaks. *Cell Cycle.* 9:389–397. https://doi.org/10.4161/cc.9.2.10475

Neelam, S., T.J. Chancellor, Y. Li, J.A. Nickerson, K.J. Roux, R.B. Dickinson, and T.P. Lele. 2015. Direct force probe reveals the mechanics of nuclear homeostasis in the mammalian cell. *Proc. Natl. Acad. Sci. USA.* 112: 5720–5725. https://doi.org/10.1073/pnas.1502111112

Nekrasova, O.E., M.G. Mendez, I.S. Chernoivanenko, P.A. Tyurin-Kuzmin, E.R. Kuczmarski, V.I. Gelfand, R.D. Goldman, and A.A. Minin. 2011. Vimentin intermediate filaments modulate the motility of mitochondria. *Mol. Biol. Cell.* 22:2282–2289. https://doi.org/10.1091/mbc.e10-09-0766

Nia, H.T., M. Datta, G. Seano, P. Huang, L.L. Munn, and R.K. Jain. 2018. Quantifying solid stress and elastic energy from excised or in situ tumors. *Nat. Protoc.* 13:1091–1105. https://doi.org/10.1038/nprot.2018.020

Otsu, N. 1979. A threshold selection method from gray-level histogram. *IEEE Trans. Syst. Man Cybern.* 9:62–66.

Patteson, A.E., K. Pogoda, F.J. Byfield, K. Mandal, Z. Ostrowska-Podhorodecka, E.E. Charrier, P.A. Galie, P. Deptuła, R. Bucki, C.A. McCulloch, and P.A. Janmey. 2018. Loss of vimentin intermediate filaments decreases peri-nuclear stiffness and enhances cell motility through confined spaces. *bioRxiv.* Preprint. https://doi.org/10.1101/371047

Raab, M., M. Gentili, H. de Belly, H.R. Thiam, P. Vargas, A.J. Jimenez, F. Lautenschlaeger, R. Voituriez, A.M. Lennon-Duménil, N. Manel, and M. Piel. 2016. ESCRT III repairs nuclear envelope ruptures during cell migration to limit DNA damage and cell death. *Science.* 352:359–362. https://doi.org/10.1126/science.aad7611

Ramsingh, R., A. Grygorczyk, A. Solecki, L.S. Cherkaoui, Y. Berthiaume, and R. Grygorczyk. 2011. Cell deformation at the air-liquid interface induces Ca2+-dependent ATP release from lung epithelial cells. *Am. J. Physiol. Lung Cell. Mol. Physiol.* 300:L587–L595. https://doi.org/10.1152/ajplung.00345.2010

Rico, F., P. Roca-Cusachs, N. Gavara, R. Farré, M. Rotger, and D. Navajas. 2005. Probing mechanical properties of living cells by atomic force microscopy with blunted pyramidal cantilever tips. *Phys Rev E Stat Nonlin Soft Matter Phys.* 72(2 Pt 1):21914. . https://doi.org/10.1103/PhysRevE.72.021914

Sackmann, E. 1994. The seventh Datta Lecture. Membrane bending energy concept of vesicle- and cell-shapes and shape-transitions. *FEBS Lett.* 346:3–16. https://doi.org/10.1016/0014-5793(94)00484-6

Sarria, A.J., J.G. Lieber, S.K. Nordeen, and R.M. Evans. 1994. The presence or absence of a vimentin-type intermediate filament network affects the shape of the nucleus in human SW-13 cells. *J. Cell Sci.* 107:1593–1607.

Satelli, A., and S. Li. 2011. Vimentin in cancer and its potential as a molecular target for cancer therapy. *Cell. Mol. Life Sci.* 68:3033–3046. https://doi.org/10.1007/s00018-011-0735-1

Seireg, A., and R.J. Arvikar. 1975. The prediction of muscular lad sharing and joint forces in the lower extremities during walking. *J. Biomech.* 8: 89–102. https://doi.org/10.1016/0021-9290(75)90089-5

Shabbir, S.H., M.M. Cleland, R.D. Goldman, and M. Mrksich. 2014. Geometric control of vimentin intermediate filaments. *Biomaterials.* 35:1359–1366. https://doi.org/10.1016/j.biomaterials.2013.10.008

Shimi, T., K. Pfleghaar, S. Kojima, C.G. Pack, I. Solovei, A.E. Goldman, S.A. Adam, D.K. Shumaker, M. Kinjo, T. Cremer, and R.D. Goldman. 2008. The A- and B-type nuclear lamin networks: microdomains involved in chromatin organization and transcription. *Genes Dev.* 22:3409–3421. https://doi.org/10.1101/gad.1735208

Shulman, Z., A.D. Gitlin, J.S. Weinstein, B. Lainez, E. Esplugues, R.A. Flavell, J.E. Craft, and M.C. Nussenzweig. 2014. Dynamic signaling by T follicular helper cells during germinal center B cell selection. *Science.* 345: 1058–1062. https://doi.org/10.1126/science.1257861

Stephens, A.D., E.J. Banigan, S.A. Adam, R.D. Goldman, and J.F. Marko. 2017. Chromatin and lamin A determine two different mechanical response regimes of the cell nucleus. *Mol. Biol. Cell.* 28:1984–1996. https://doi.org/10.1091/mbc.e16-09-0653

Stephens, A.D., P.Z. Liu, E.J. Banigan, L.M. Almassalha, V. Backman, S.A. Adam, R.D. Goldman, and J.F. Marko. 2018. Chromatin histone modifications and rigidity affect nuclear morphology independent of lamins. *Mol. Biol. Cell.* 29:220–233. https://doi.org/10.1091/mbc.E17-06-0410

Swift, J., I.L. Ivanovska, A. Buxboim, T. Harada, P.C.D.P. Dingal, J. Pinter, J.D. Pajerowski, K.R. Spinler, J.W. Shin, M. Tewari, et al. 2013. Nuclear lamin-A scales with tissue stiffness and enhances matrix-directed differentiation. *Science.* 341:1240104. https://doi.org/10.1126/science.1240104

Thiery, J.P., H. Acloque, R.Y.J. Huang, and M.A. Nieto. 2009. Epithelial-mesenchymal transitions in development and disease. *Cell.* 139: 871–890. https://doi.org/10.1016/j.cell.2009.11.007

Turgay, Y., M. Eibauer, A.E. Goldman, T. Shimi, M. Khayat, K. Ben-Harush, A. Dubrovsky-Gaupp, K.T. Sapra, R.D. Goldman, and O. Medalia. 2017. The molecular architecture of lamins in somatic cells. *Nature.* 543:261–264. https://doi.org/10.1038/nature21382

Vahabikashi, A., C.Y. Park, K. Perkumas, Z. Zhang, E.K. Deurloo, H. Wu, D.A. Weitz, W.D. Stamer, R.D. Goldman, J.J. Fredberg, and M. Johnson. 2019. Probe Sensitivity to Cortical versus Intracellular Cytoskeletal Network Stiffness. *Biophys. J.* 116:518–529. https://doi.org/10.1016/j.bpj.2018.12.021

Vargas, J.D., E.M. Hatch, D.J. Anderson, and M.W. Hetzer. 2012. Transient nuclear envelope rupturing during interphase in human cancer cells. *Nucleus.* 3:88–100. https://doi.org/10.4161/nucl.18954

Wilhelmsen, K., S.H.M. Litjens, I. Kuikman, N. Tshimbalanga, H. Janssen, I. van den Bout, K. Raymond, and A. Sonnenberg. 2005. Nesprin-3, a novel outer nuclear membrane protein, associates with the cytoskeletal linker protein plectin. *J. Cell Biol.* 171:799–810. https://doi.org/10.1083/jcb.200506083

Xia, Y., I.L. Ivanovska, K. Zhu, L. Smith, J. Irianto, C.R. Pfeifer, C.M. Alvey, J. Ji, D. Liu, S. Cho, et al. 2018. Nuclear rupture at sites of high curvature compromises retention of DNA repair factors. *J. Cell Biol.* 217:3796–3808. https://doi.org/10.1083/jcb.201711161

Yang, J., and R.A. Weinberg. 2008. Epithelial-mesenchymal transition: at the crossroads of development and tumor metastasis. *Dev. Cell.* 14:818–829. https://doi.org/10.1016/j.devcel.2008.05.009